# Origin of Monochromatic Electron Emission From Planar-Type Graphene/*h*-BN/*n*-Si Devices

Tomoya Igari,[1,2] Masayoshi Nagao,[2] Kazutaka Mitsuishi,[3] Masahiro Sasaki,[1,4] Yoichi Yamada,[1,*] and Katsuhisa Murakami[2,†]

[1] *Faculty of Pure and Applied Sciences, University of Tsukuba, 1-1-1 Ten-nodai, Tsukuba, Ibaraki 305-8577, Japan*
[2] *Device Technology Research Institute, National Institute of Advanced Industrial Science and Technology (AIST), 1-1-1 Umezono, Tsukuba, Ibaraki 305-8568, Japan*
[3] *National Institute for Materials Science, 1-2-1 Sengen, Tsukuba, Ibaraki 305-0047, Japan*
[4] *Tsukuba Research Center for Energy Materials Science (TREMS), University of Tsukuba, 1-1-1 Ten-nodai, Tsukuba, Ibaraki 305-8577, Japan*

(Received 24 August 2020; accepted 21 December 2020; published 25 January 2021)

We previously reported highly monochromatic electron emission from the planar-type electron emission devices based on a graphene/hexagonal boron nitride (*h*-BN) heterostructure. In this paper, the electron energy distribution (EED) of these devices is examined to clarify the mechanism of monochromatic electron emission. We find that the monochromaticity of the electron beam depends significantly on the electronic structure of the substrate material; for the devices with an *n*-type silicon substrate, the narrowest FWHM of the electron beam is 0.18 eV, whereas that of devices with a metallic (Nb) substrate is 0.33 eV. At the same time, simulations considering the electron scattering by phonons acceptably reproduced the shape of each EED spectrum considering the small energy loss due to out-of-plane acoustic phonon modes in *h*-BN. Thus, the monochromatic electron emission from the graphene/*h*-BN/*n*-Si device is ascribed to a combination of the narrow energy distribution of electrons at the conduction band of the *n*-Si substrate and small phonon energy of the *h*-BN insulating layer. These features also realize the excellent emission properties in addition to the monochromaticity of the beam, such as a high emission current density of 9.3A/cm$^2$, insensitivity to environmental pressure up to 10 Pa, and long lifetime of more than 7 days with little decay.

DOI: 10.1103/PhysRevApplied.15.014044

## I. INTRODUCTION

Electron-beam (EB) applications such as electron microscopy and EB lithography have been widely used in numerous industries and academic studies, and the electron source is the most upstream component of the EB devices. Widely commercialized electron sources are classified as three types according to their operation principle: thermionic emission (TE) cathodes [1], cold-field-emission (CFE) cathodes [2,3], and Schottky-emission (SE) cathodes [4,5]. Although TE cathodes are relatively inexpensive and stable under relatively low vacuum, TE cathodes need high temperature in operation and emitted electrons have a broad energy spread of more than 2 eV [6]. CFE cathodes have numerous benefits for EB applications, such as high brightness of $10^9$ A/cm$^2$ sr at 20 kV and narrow energy spread of 0.3 eV [6]. However, because of the chemical and physical instability of the tip with extremely small curvature, CFE sources need ultrahigh vacuum (UHV) conditions and a flashing process to clean their emission plane [7]. SE cathodes are electron sources that achieve stable electron emission and a relatively small energy spread of 0.3–1.0 eV [6], but require both high temperature and high extraction field. These requirements of the commercialized electron sources, such as high extraction voltage, UHV environments and high temperature, make electron guns complex and expensive. For electron microscopy and EB lithography, the energy spread of the emitted EB is also critical for their spatial resolution because of the chromatic aberration of electron lenses [8]. Therefore, an inexpensive electron source that achieves high emission current with small energy spread, low operating voltage and the stability in the low vacuum is desired for next-generation EB applications.

Planar-type electron emission devices are promising alternative electron sources. A planar-type device has a sandwich structure in which a thin insulating material is located between two conductors, i.e., metal-insulator-metal [9–11] and metal-oxide-semiconductor [12–17] structures. These devices potentially have excellent features such as low operating voltage, operation

*yamada@bk.tsukuba.ac.jp
†murakami.k@aist.go.jp

 © 2021 American Physical Society

under low vacuum, and small divergence angle of the EB. However, the conventional planar electron sources also have critical disadvantages of the broad energy spread of the EB and low emission efficiency, which have hampered the practical use of the planar devices. Both of these disadvantages in the planar devices are mainly caused by the inelastic scattering of electrons in the insulating layer and the top gate electrode [12,14]. When a gate voltage is applied to a gate electrode, the potential barrier width decreases because of the high field and electrons tunnel through the potential barrier by quantum tunneling [18]. In the planar electron source, electrons have to travel through the conduction band of the insulating layer and top gate electrode, where they lose their energy by scattering [19]. One strategy to narrow the energy spread of the EB from planar-type electron sources is thus to suppress the inelastic scattering of electrons in the insulating layer and gate electrode. Recently, planar electron emission devices using graphene gate electrodes have been developed to suppress electron scattering in the gate electrode [20–25]. A so-called graphene-oxide-semiconductor (GOS) device realized a high emission efficiency of 48.5% because electron scattering in the graphene gate electrode was suppressed [26]. Thus, graphene is a suitable material for use as the gate electrode of planar electron sources because of its high electron transmittance [27,28]. However, electron scattering within the oxide layer [29] of GOS devices still widens the energy spread. In fact, despite the graphene gate electrode drastically suppressing electron scattering, a broad electron energy distribution (EED) spectrum of more than 1 eV was observed from a GOS emission device [25].

On the other hand, in our previous study, we constructed a device with a structure of graphene/hexagonal boron nitride (*h*-BN)/*n*-type silicon (*n*-Si) in order to suppress electron scattering in the insulating layer [30]. This device realized a high emission current of 2.4 A/cm$^2$ and small EB energy spread of around 0.28 eV. The insulator *h*-BN [31–33] has an atomically flat surface and small lattice mismatch with graphene, which allows these materials to form a sharp interface with graphene electrode [34]. In addition, the electron scattering cross section of *h*-BN, which consists of light elements of nitrogen and boron, should be smaller than that of the conventional silicon dioxide ($SiO_2$). However, the details of the origin of monochromatic electron emission, such as the scattering source within the insulating layer and inelastic mean free path (IMFP) of electrons in the insulating layer, have not been clarified. In particular, little is known about the inelastic scattering properties of low-energy electrons (less than 50 eV) in *h*-BN. The IMFP of electrons with energies above 50 eV in *h*-BN has been investigated both experimentally [35] and by a theoretical simulation [36].

In this paper, in order to discuss the origin of the highly monochromatic electron emission from our graphene/*h*-BN/*n*-Si emission device, EED spectra from these devices are systematically measured and analyzed in detail by theoretical simulations considering the electron scattering caused by phonons in the insulating layer. To examine the effect of the initial electron distribution of the substrate on EED spectra, we fabricate the graphene/*h*-BN devices with semiconducting (*n*-Si) and metallic (Nb) substrates and find that EED spectra clearly reflected the electron distribution of the substrate. This finding suggests that the electron scattering within the *h*-BN layer and graphene electrode is indeed so small that the initial electron energy distribution in the substrate can determine the energy width of the emitted electron beam. The fitting of the EED spectra by the theoretical simulations indicates that the low-energy, out-of-plane vibration (ZA) modes in *h*-BN are responsible for the inelastic electron scattering, which makes the total energy loss of the emitted electrons in the *h*-BN layer significantly smaller. The suppressed electron scattering is also beneficial to prevent the breakdown of the device, which leads to a long lifetime of more than 7 days. In addition, it is found that the graphene/*h*-BN/*n*-Si device exhibits narrow energy spread of 0.68 eV even at a high emission current density of 9.3 A/cm$^2$, and these emission properties are insensitive to the environmental pressure up to 10 Pa.

## II. EXPERIMENTAL AND THEORETICAL METHODS

The graphene/*h*-BN/*n*-Si device is fabricated as follows. An *n*-type Si substrate (2–5 Ω cm) with a 300-nm-thick thermal oxide layer is prepared as a starting substrate. An electron emission area of $10 \times 10$ $\mu$m is formed by photolithography and buffered hydrofluoric acid (BHF) etching. A *h*-BN insulating layer is formed on the *n*-Si substrate by the dry-transfer technique. A graphene top gate is directly synthesized on the *h*-BN layer by PECVD at 700 °C. To isolate each emission area in the substrate, the graphene electrode and *h*-BN layer are partially etched using $O_2$ plasma etching and $SF_6$ reactive ion etching, respectively. A Ni (100 nm)/Ti (10 nm) contact electrode is fabricated by photolithography, EB evaporation, and a lift-off process. To connect with the substrate, a Ni/Ti back contact electrode is fabricated. Details of the fabrication processes have been described elsewhere [30].

The graphene/*h*-BN/Nb device is fabricated as follows. The starting substrate is *n*-Si with a 300-nm-thick thermal oxide layer, which is the same as that used in the graphene/*h*-BN/*n*-Si device. A Nb underlayer with a thickness of 200 nm is deposited on the entire surface of the substrate by dc sputtering. A $SiO_2$ field insulator layer with a thickness of 300 nm is deposited on the Nb underlayer by PECVD using tetraethoxysilane. Subsequent fabrication processes are the same as those for the graphene/*h*-BN/*n*-Si emission device except for the

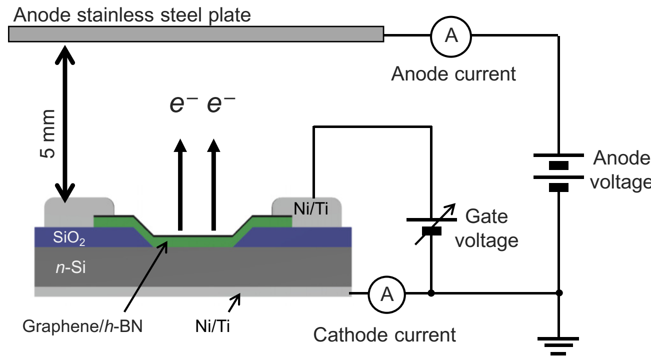


FIG. 1. Schematic diagram of the measurement system for the electron emission properties of graphene/$h$-BN electron emission devices.

formation of a contact hole for the back contact. The emission area is patterned by photolithography and BHF etching. A h-BN insulating layer and graphene gate electrode are formed by dry transfer and PECVD, respectively. Graphene and $h$-BN are partially etched to isolate the device. To connect with the Nb underlayer from the surface of the substrate, a contact hole with dimensions of $150\times150$ $\mu$m is patterned by photolithography and BHF etching. A Ni/Ti contact electrode is then fabricated by EB evaporation.

The fundamental emission properties of the devices are measured at a pressure of $10^{-6}$ Pa using the setup depicted in Fig. 1. Before the measurement, the devices are annealed at 400 °C in a vacuum chamber at a pressure of $10^{-5}$ Pa to remove residual photoresist on the graphene gate electrode. An anode plate at a voltage of 1 kV is placed 5 mm from the device to collect emitted electrons. Emission efficiency $\eta$ is defined as the following equation, using anode current $I_a$ and cathode current $I_c$:

$$\eta = \frac{I_a}{I_c}. \tag{1}$$

Energy analysis of electrons emitted from the device is performed using a hemispherical electron energy analyzer at a pressure of $10^{-6}$ Pa. Emitted electrons are selected with a probe hole in an anode plate in front of the analyzer. The probe hole is located 20 mm from the device surface and a voltage of 2.5 kV is applied to accelerate the EB.

The theoretical simulation of the energy distribution of emitted electrons is conducted using a combination of Fowler-Nordheim (FN) tunneling [18] and the macroscopic scattering model of phonons in the insulating layer, as shown in Fig. 2. We divide the one-dimensional simulation model into four regions. In the case of the graphene/$h$-BN/$n$-Si structure, we consider the energy distribution of electrons at the conduction band of the semiconductor, which is given by the product of the Fermi-Dirac distribution $f(E)$ and density of states of the conduction band

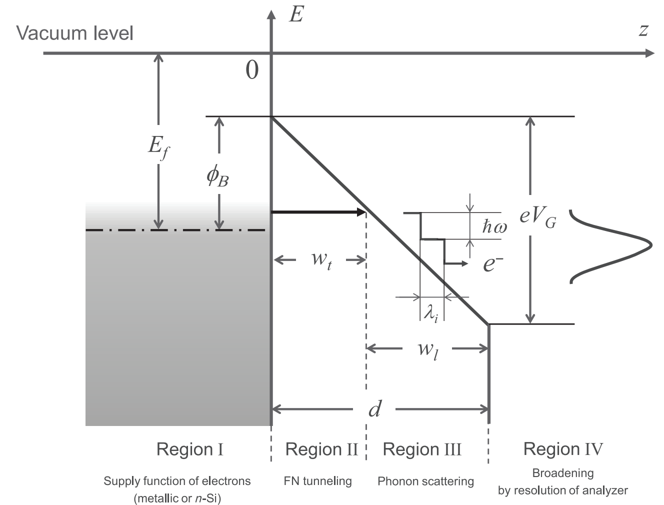


FIG. 2. Simulation model of planar-type electron emission devices with a structure of graphene/$h$-BN/Nb or graphene/$h$-BN/$n$-Si.

[37] as a supply function as follows:

$$E(E) = \frac{1}{2\pi^2}\left(\frac{2m}{\hbar}\right)^{3/2}\frac{(E-E_c)^{1/2}}{1+\exp[-(E-E_f)/kT]}, \tag{2}$$

where $k$, $T$, $E_f$, and $E_c$ are the Boltzmann constant, temperature, Fermi energy of the substrate, and energy of the bottom of the conduction band in the Si substrate, respectively. In the case of the graphene/$h$-BN/Nb device, region 1 is the supply function of electrons $E(E)$, which is $f(E)$ and written as follows:

$$E(E) = \frac{1}{1+\exp[(E-E_f)/kT]}. \tag{3}$$

In region 2, the energy distribution of electrons injected into the conduction band of the insulating layer via FN tunneling $U(E)$ is calculated by multiplying the supply function $E(E)$ and transmission probability $T(E)$ as follows:

$$T(E) = \exp\left[-\frac{8\pi\sqrt{2m}}{3heF}(\phi_B - E)^{\frac{3}{2}}\right], \tag{4}$$

where $h$, $e$, $F$, $m$, and $\phi_B$ are the Planck constant, elementary charge, electric field applied to the insulator, effective mass of electrons in the insulating layer, and barrier height at the interface between the substrate and insulating layer, respectively. The calculations are conducted using effective masses of 0.26 $m_e$ and 0.40 $m_e$ ($m_e$ is mass of a resting electron) for the $h$-BN [38] and $SiO_2$ [18] insulating layers, respectively. In region 3, the scattering phenomena by phonons while electrons travel through the conduction band of the insulating layer are considered. We consider

the scattering processes by phonons with an energy of $\hbar\omega$. When an electron with an energy of $E$ is scattered by a phonon with an energy of $\hbar\omega$, the scattered electron distribution $D(\varepsilon)$ is calculated using the mean free path of electrons in the insulator $\lambda_i$ [29,39,40],

$$D(\varepsilon) = \frac{1}{\hbar\omega\sqrt{2\pi(w_l/\lambda_i)}} \exp\left(-\frac{\{\varepsilon - [E - \hbar\omega(w_l/\lambda_i)]\}^2}{2(\hbar\omega)^2(w_l/\lambda_i)}\right), \tag{5}$$

where $w_l$ is the travel distance of electrons in the conduction band of the insulator, which is given by $w_l = d - \phi_B/eF$. Therefore, the distribution of electrons arriving at the insulating layer-gate electrode interface $I(E)$ is obtained as the convolution of $(U \times D)(\varepsilon)$. Because inelastic scattering in the graphene gate electrode is negligible [26], the effect of scattering in the gate electrode is not considered. Thus, in region 4, we only consider the effect of spectrum broadening by the resolution function of the electron energy analyzer. The EED of the emitted EB is finally calculated as the convolution of the resolution function and $I(E)$. The resolution function of the analyzer $R(\tau - E)$ is written as

$$R(\tau - E) = \frac{1}{2r\sqrt{\pi}} \exp\left[\frac{(\tau - E)^2}{2r^2}\right], \tag{6}$$

where $r$ is the FWHM of the Gaussian distribution. The resolution of hemispherical energy analyzer $r$ is taken to be 30 meV according to the manufacturer specifications.

The electron emission properties of the fabricated devices are measured in a vacuum chamber at different pressures of $10^{-6}$ and $10^{-4}$ Pa, which are formed by varying the evacuation velocity via turbomolecular and scroll pumps. The atmospheres of $10^{-1}$ and 10 Pa are formed by evacuation using a turbomolecular pump and/or scroll pump after purging with $N_2$. To prevent electric discharge, the anode voltage is lowered to 200 V during the measurements at pressures of $10^{-1}$ and 10 Pa.

## III. RESULTS AND DISCUSSION

First, we characterize the current-voltage ($I$-$V$) properties of the graphene/$h$-BN devices on semiconducting ($n$-Si) and metallic (Nb) substrates. Figures 3(a) and 3(b)

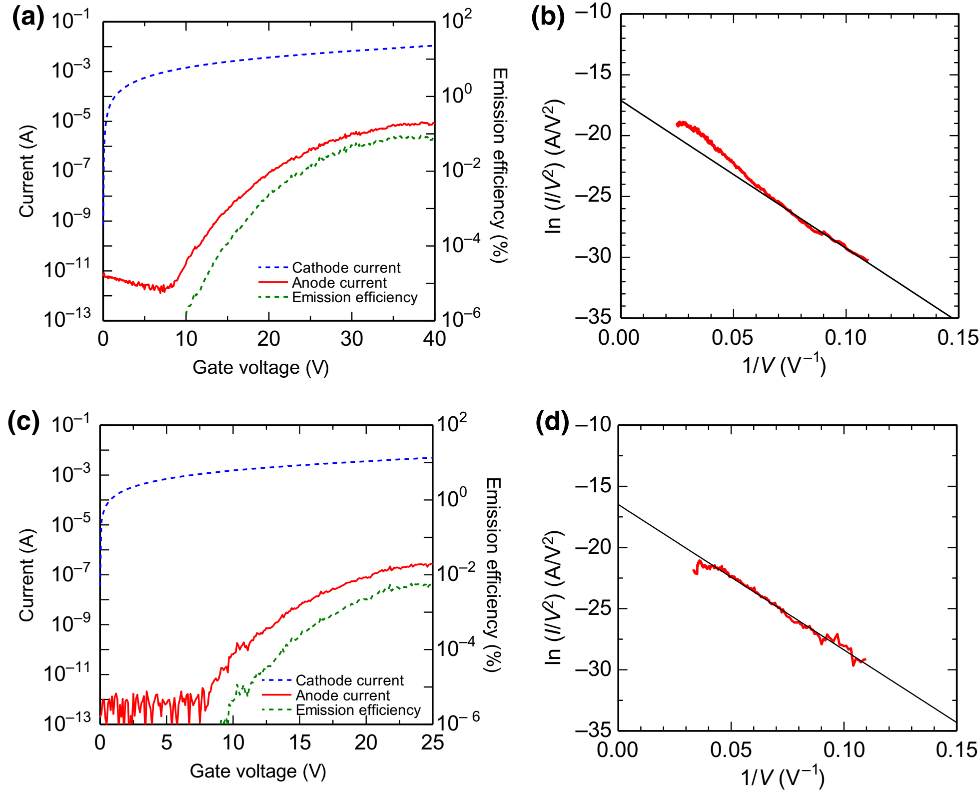


FIG. 3. (a) Electron emission characteristics and (b) FN plots of anode current for the graphene/$h$-BN/$n$-Si device. (c) Electron emission characteristics and (d) FN plots of anode current for the graphene/$h$-BN/Nb device. Blue dashed, red solid, and green dashed lines indicate cathode current, anode current, and emission efficiency, respectively.

show the electron emission characteristics and anode current, which is replotted as a FN plot, of the graphene/*h*-BN/*n*-Si device. The maximum emission current is 9.3 $\mu$A, which corresponds to a current density of 9.3 A/cm$^2$. This maximum current density is several times higher than a previously reported value [30]. The high current density is caused by the decreased thickness of the *h*-BN insulating layer in the present device; the thickness of the *h*-BN layer estimated from the slope of the FN curve is 6.44 nm, which is 2.11 nm thinner than that of our previously reported device [30]. Note that the anode current in the gate voltage region of 0 to 8 V showed a slight decrease of a few pA, which is due to the noise signal possibly originating from the remaining charge in the coaxial cable. The maximum emission efficiency of this device is 0.088%. The reason for this small efficiency is the large leakage current resulting from the defects such as cracks and wrinkles of the *h*-BN film. We note that the deviation from the linear behavior in the FN plot at a high gate voltage regime in Fig. 3(b) is due to voltage drop caused by the leakage current. Further optimization of the uniformity of the *h*-BN layer is surely required to reduce the leakage current, which would drastically improve the emission efficiency. We show that by refining the device structure, maximum efficiency of this type of device can be increased up to 70% [26].

Figures 3(c) and 3(d) show the electron emission characteristics and FN plot of the anode current from the graphene/*h*-BN/Nb emission device. The emission characteristics are found to be similar to those of the graphene/*h*-BN/*n*-Si device. The maximum anode current is 0.27 $\mu$A, which corresponds to a current density of 0.27 A/cm$^2$. Note that the maximum gate voltage examined for the graphene/*h*-BN/Nb device is smaller than the case of the graphene/*h*-BN/*n*-Si device, due to smaller breakdown voltage resulting from slightly thinner insulating layer thickness. The thickness of the *h*-BN insulating layer estimated from the slope of the FN plot is 6.00 nm. The maximum emission efficiency of this device is 0.006%. Again, the small efficiency is due to the leakage current.

The time drift of the anode current for the graphene/*h*-BN/*n*-Si emission device during dc operation at a gate voltage of 30 V is shown in Fig. 4(a). Only a slight decay of the anode current is observed, and the device did not break during continuous operation for 7 days. The lifetime of the device is longer than that of conventional planar-type electron emission devices, which is anticipated in our previous report [30]. Such a long lifetime is a signature of the small scattering in the *h*-BN layer because inelastic scattering by hot electrons in the insulator is one of the mechanisms for electric breakdown [39,41]. Although considerable fluctuation of the anode current is observed during the long-term experiment, the fluctuation is as small as 7.9% during a short-term measurement, as displayed in Fig. 4(b). In addition, the anode current from the graphene/*h*-BN/*n*-Si emission device did not depend on the ambient pressure in the range of $10^{-6}$ to 10 Pa, as shown in Fig. 5, which is one of the virtues of planar electron emission devices.

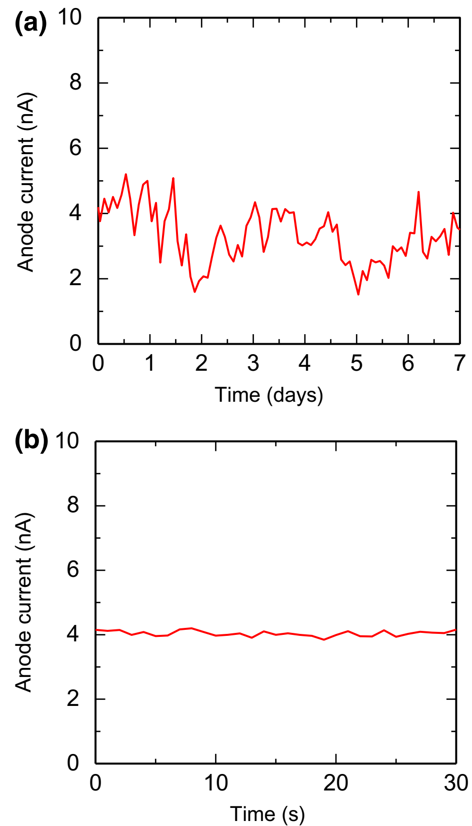


FIG. 4. Time drift of anode current for the graphene/*h*-BN/*n*-Si emission device during dc operation (gate voltage: 30 V).

The EED spectra for the graphene/*h*-BN/*n*-Si and graphene/*h*-BN/Nb emission devices are presented in Figs. 6(a) and 6(b), respectively. For the graphene/*h*-BN/*n*-Si device, the FWHM of the EED spectrum at a gate voltage of 25 V is 0.18 eV. This value is extremely small compared with those of conventional CFE and SE cathodes, as we have previously reported [30]. In contrast, in the case of the device with a metallic (Nb) substrate, the FWHM of the EED spectrum at a gate voltage of 9.3 V is 0.33 eV, which is comparable with that of a CFE tip [6]. Here, it is also useful to focus on the characteristic shape of these EED curves. In particular, in the case of the device with *n*-Si substrate, the shape of the EED spectra with a tail on the high-energy side is unique among those of conventional CFE devices. This characteristic shape of the EED spectrum resembles the electron distribution at the conduction band of the *n*-Si substrate. On the other hand, in the case of the device with metallic (Nb) substrate, the shape of the EED spectra, which had a tail on the low-energy side, is similar to that in the case of conventional CFE from a metallic tip [3,42]. The observed difference in

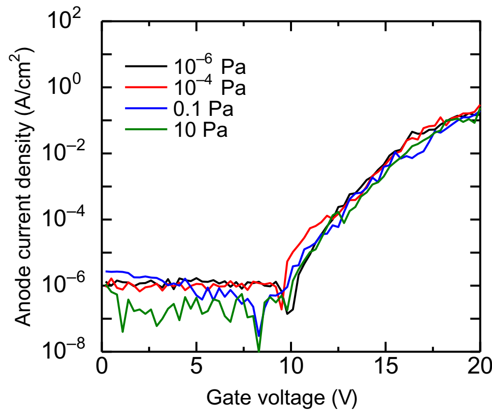


FIG. 5. Anode current density for the graphene/$h$-BN/$n$-Si device at different pressures.

the shape of the EED spectra for the graphene/$h$-BN/$n$-Si and graphene/$h$-BN/Nb devices should be related to the different electron distributions in the substrate. It is considered that the very sharp EED spectrum with characteristic spectral shape observed for the device on the $n$-Si substrate reflects the narrow electron distribution in the conduction band, whereas the moderate width and conventional shape of the EED spectra of the device on a Nb substrate is a consequence of its metallic electronic structure. Thus, it can be considered that the EED spectra of these devices reflects the electronic structure of the substrate. This fact suggests that the electron scattering within the $h$-BN layer and graphene electrode is so small and the electrons around the uppermost energy in the substrate can be emitted without significant broadening in the energy. This is in clear contrast to the behavior of a device with a conventional $SiO_2$ insulating layer. Figure 6(c) shows the simulated and measured EED spectra of a graphene/$SiO_2$/$n$-Si (GOS) device [25]. For the GOS device, the FWHM of its EED spectrum at a gate voltage of 9.06 eV is 1.1 eV. In addition, the spectrum is symmetric, unlike the case for the devices with $h$-BN insulating layers. This result indicates that the inelastic electron scattering in the $SiO_2$ layer obscures the information of the initial electron distribution in the substrate, and this effect can be largely suppressed when $h$-BN is used instead of $SiO_2$.

To estimate the effect of the inelastic scattering within the $h$-BN insulating layer, theoretical simulations of the electron emission behavior of the present graphene/$h$-BN/$n$-Si and graphene/$h$-BN/Nb devices taking the phonon energy and electron mean free path into account are conducted. Because the electron scattering in the graphene electrode is shown to be negligible and constant for all the devices examined here, we focus on the scattering effect in the $h$-BN layer. For the electron emission from graphene/$h$-BN/$n$-Si and graphene/$h$-BN/Nb devices, we simulate the scattering of the electrons in $h$-BN layers with thicknesses of 6.44 and 6.00 nm, respectively. For the initial electron distributions in the $n$-Si and Nb substrates, we use the results obtained from Eqs. (2) and (3), respectively, which are shown as dashed lines in Fig. 6. The best fitting of the experimental spectra for both graphene/$h$-BN/$n$-Si and graphene/$h$-BN/Nb devices is obtained with a phonon energy $\hbar\omega$ of 0.04 eV and IMFP $\lambda_i$ of 1.0 nm, as indicated by the solid lines in Fig. 6. The spectral shape is reasonably reproduced by the theoretical simulation with parameters of $\hbar\omega = 0.04$ [eV] and $\lambda_i = 1.0$ [nm]. An IMFP of 1.0 nm is considered to be a physically reasonable value based on the Penn algorithm [36]. The phonon energy of 0.04 eV corresponds to the reported phonon energy of the out-of-plane acoustic (ZA) phonon mode of $h$-BN with larger density of states [43]. In both graphene/$h$-BN/$n$-Si and graphene/$h$-BN/Nb devices, the total energy loss caused by scattering events is small enough that the emission spectra largely

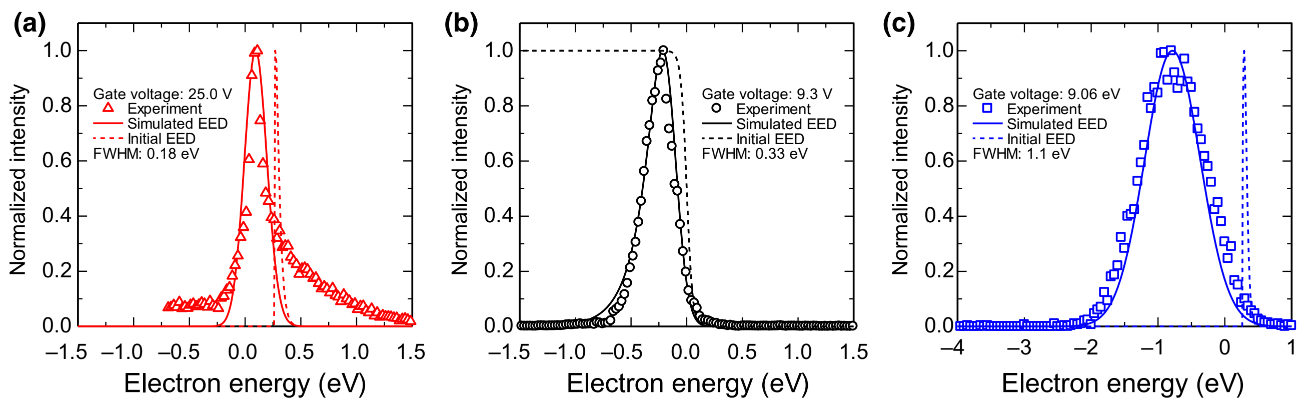


FIG. 6. Comparison of experimental (dots), simulated (solid line) electron energy distribution (EED), electron distribution in the substrate (initial EED, dashed lines) spectra for graphene/$h$-BN devices with (a) $n$-Si and (b) Nb substrates. Fitting parameters $\hbar\omega$ and $\lambda_i$ are 0.04 eV and 1.0 nm, respectively. (c) Comparison of experimental and simulated EED spectra for a graphene/$SiO_2$/$n$-Si structure. Fitting parameters are $\hbar\omega = 0.15$ [eV] and $\lambda_i = 0.9$ [nm].

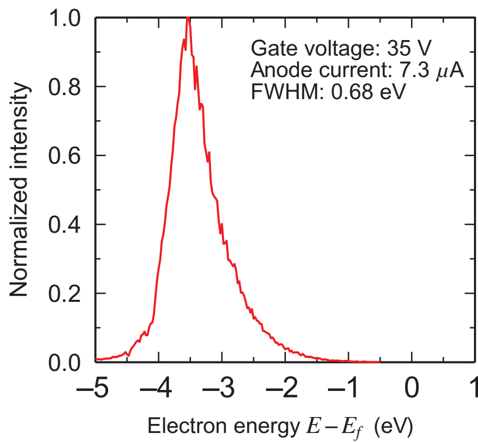


FIG. 7. Energy spectrum of emitted electrons from a graphene/$h$-BN/$n$-Si emission device at a gate voltage of 35 V.

reflected the original electron distribution in the substrates. However, a further sophisticated model is needed to fully reproduce the tail shape of EED spectra in the device with an $n$-Si substrate.

As shown in Fig. 6(c), the EED spectrum for the graphene/$SiO_2$/$n$-Si (GOS) structure [25], in which the thickness of the $SiO_2$ layer is 10.0 nm, is fitted using parameters of $\hbar\omega = 0.15$ [eV] and $\lambda_i = 0.9$ [nm]. In this case, the substantial scattering changed the shape of the electron distribution of the $n$-Si substrate, in clear contrast to the case for the devices with $h$-BN. The IMFP of 0.9 nm for the device with a $SiO_2$ insulating layer is comparable with that of the devices with $h$-BN. In contrast, the phonon energy of 0.15 eV corresponds to the longitudinal optical phonon mode of amorphous $SiO_2$ [44,45]. Thus, the fitting of the EED spectrum for the GOS device is also physically reasonable. It is notable that the phonon energy in the device with a $SiO_2$ insulating layer is 3.8 times larger than that of the devices with $h$-BN. These results indicate that the greatly suppressed inelastic scattering in the $h$-BN insulating layer is owing to the low energy of the ZA phonon mode of $h$-BN, which is considered to mainly interact with the low-energy electrons traveling vertically through the atomic layers of $h$-BN. Therefore, it can be concluded that the almost monochromatic electron emission from the graphene/$h$-BN/$n$-Si structure is caused by the combination of the narrow energy spread of electrons at the conduction band of the low-doped $n$-Si, and limited electron scattering in the $h$-BN insulating layer. The detailed analysis of the dependence of the emission current on the doping level of the substrate is now underway.

These characteristics of the present graphene/$h$-BN/$n$-Si devices made it possible for them to emit a larger current with small energy spread, as demonstrated at an elevated gate voltage of 35 V (Fig. 7). The anode current density in this case is as high as 7.3 A/$cm^2$ and the FWHM is only 0.68 eV. Note that at this extremely high gate voltage, the EED peak shifts to lower energy than that at lower gate voltage because of the potential drop caused by the large leakage current of a few milliamperes. These results indicate that the graphene/$h$-BN/$n$-Si electron emission devices, realizing large current density with relatively small energy spread, are promising for EB applications.

## IV. CONCLUSIONS

To discuss the origin of the almost monochromatic electron emission from planar-type electron emission devices based on a graphene/$h$-BN structure, their electron energy spectra are systematically measured and analyzed by theoretical simulations considering the electron scattering caused by phonons in the $h$-BN insulating layer. Comparison of the EED spectra of graphene/$h$-BN devices with semiconducting ($n$-Si) and metallic (Nb) substrates revealed that the EED clearly reflected the electron distribution of the substrate, unlike the case for conventional devices with a $SiO_2$ insulating layer. The fitting of EED spectra indicated that the ZA phonons in $h$-BN are responsible for the inelastic scattering of low-energy electrons, which decreased the total energy loss of the emitted electrons in the graphene/$h$-BN devices. It is concluded that the almost monochromatic electron emission from the graphene/$h$-BN/$n$-Si structure is caused by a combination of the narrow energy spread of electrons at the conduction band of the $n$-Si substrate and small inelastic scattering in the $h$-BN insulating layer. The graphene/$h$-BN/Si device displays a high emission current density of 9.3 A/$cm^2$, small energy spread of 0.68 eV with high emission current, long lifetime of more than 7 days, and insensitivity to environmental pressure up to 10 Pa.

## ACKNOWLEDGMENTS

This work is partly supported by JSPS KAKENHI Grants No. 15H05522, No. 16K14223, No. 18H01505, No. 18K18910, No. 19K05182, and No. 19K04516. This work is done as part of JAXA/RDD's active space-debris removal researches. Support is also received from AIST Nanofabrication Platform, University of Tsukuba Nanofabrication Platform, and NIMS Microstructural Characterization Platform in the Nanotechnology Platform Project sponsored by the Ministry of Education, Culture, Sports, Science and Technology (MEXT), Japan.

[1] M. E. Haine and P. A. Einstein, Characteristics of the hot cathode electron microscope gun, Br. J. Appl. Phys. **3**, 40 (1952).

[2] A. V. Crewe, J. Wall, and L. M. Welter, A high-resolution scanning transmission electron microscope, J. Appl. Phys. **39**, 5861 (1968).

[3] R. Gomer, *Field Emission and Field Ionization* (American Institute of Physics, New York, NY, 1993).
[4] H. S. Kim, M. L. Yu, M. G. R. Thomson, E. Kratschmer, and T. H. P. Chang, Energy distributions of Zr/O/W Schottky electron emission, J. Appl. Phys. **81**, 461 (1997).
[5] L. W. Swanson and L. C. Crouser, Angular confinement of field electron and Ion emission, J. Appl. Phys. **40**, 4741 (1969).
[6] A. Bogner, P.-H. Jouneau, G. Thollet, D. Basset, and C. Gauthier, A history of scanning electron microscopy developments: Towards "wet-STEM" imaging, Micron **38**, 390 (2007).
[7] K. Kasuya, S. Katagiri, T. Ohshima, and S. Kokubo, Stabilization of a tungsten ⟨310⟩ cold field emitter, J. Vac. Sci. Technol. B **28**, L55 (2010).
[8] L. Reimer, *Scanning Electron Microscopy: Physics of Image Formation and Microanalysis* (Springer, Berlin, Heidelberg, 1985).
[9] C. A. Mead, Operation of tunnel-emission devices, J. Appl. Phys. **32**, 646 (1961).
[10] T. Kusunoki, M. Suzuki, S. Sasaki, T. Yaguchi, and T. Aida, Fluctuation-free electron emission from non-formed metal-insulator-metal (MIM) cathodes fabricated by low current anodic oxidation, Jpn. J. Appl. Phys. **32**, L1695 (1993).
[11] H. Adachi, Emission characteristics of metal–insulator–metal tunnel cathodes, J. Vac. Sci. Technol. B **14**, 2093 (1996).
[12] K. Yokoo, Emission characteristics of metal–oxide–semiconductor electron tunneling cathode, J. Vac. Sci. Technol. B **11**, 429 (1993).
[13] K. Yokoo, Energy distribution of tunneling emission from Si-gate metal–oxide–semiconductor cathode, J. Vac. Sci. Technol. *B* **12**, 801 (1994).
[14] K. Yokoo, G. Koshita, S. Hanzawa, Y. Abe, and Y. Neo, Experiments of highly emissive metal–oxide–semiconductor electron tunneling cathode, J. Vac. Sci. Technol. B **14**, 2096 (1996).
[15] H. Mimura, Y. Abe, J. Ikeda, K. Tahara, Y. Neo, H. Shimawaki, and K. Yokoo, Resonant Fowler–Nordheim tunneling emission from metal-oxide-semiconductor cathodes, J. Vac. Sci. Technol. B **16**, 803 (1998).
[16] A. Di Bartolomeo, F. Urban, M. Passacantando, N. McEvoy, L. Peters, L. Iemmo, G. Luongo, F. Romeo, and F. Giubileo, A $WSe_2$ vertical field emission transistor, Nanoscale **11**, 1538 (2019).
[17] A. Di Bartolomeo, A. Pelella, F. Urban, A. Grillo, L. Iemmo, M. Passacantando, X. Liu, and F. Giubileo, Field emission in ultrathin $PdSe_2$ back-gated transistors, Adv. Electron. Mater. **6**, 2000094 (2020).
[18] M. Lenzlinger and E. H. Snow, Fowler-Nordheim tunneling into thermally grown $SiO_2$, J. Appl. Phys. **40**, 278 (1969).
[19] R. M. Handy, Hot electron energy loss in tunnel cathode structures, J. Appl. Phys. **37**, 4620 (1966).
[20] K. Murakami, S. Tanaka, A. Miyashita, M. Nagao, Y. Nemoto, M. Takeguchi, and J. Fujita, Graphene-oxide-semiconductor planar-type electron emission device, Appl. Phys. Lett. **108**, 083506 (2016).
[21] K. Nishiguchi, D. Yoshizumi, Y. Sekine, K. Furukawa, A. Fujiwara, and M. Nagase, Planar cold cathode based on a multilayer-graphene/$SiO_2$ /Si heterodevice, Appl. Phys. Express **9**, 105101 (2016).
[22] M. P. Kirley, T. Aloui, and J. T. Glass, Monolayer graphene-insulator-semiconductor emitter for large-area electron lithography, Appl. Phys. Lett. **110**, 233109 (2017).
[23] A. Kojima, R. Suda, and N. Koshida, Improved quasiballistic electron emission from a nanocrystalline Si cold cathode with a monolayer-graphene surface electrode, Appl. Phys. Lett. **112**, 133102 (2018).
[24] K. Murakami, S. Tanaka, T. Iijima, M. Nagao, Y. Nemoto, M. Takeguchi, Y. Yamada, and M. Sasaki, Electron emission properties of graphene-oxide-semiconductor planar-type electron emission devices, J. Vac. Sci. Tech. B **36**, 02C110 (2018).
[25] K. Murakami, J. Miyaji, R. Furuya, M. Adachi, M. Nagao, Y. Neo, T. Takao, Y. Yamada, M. Sasaki, and H. Mimura, High-performance planar-type electron source based on a graphene-oxide-semiconductor structure, Appl. Phys. Lett. **114**, 213501 (2019).
[26] K. Murakami, M. Adachi, J. Miyaji, R. Furuya, M. Nagao, Y. Yamada, Y. Neo, Y. Takao, M. Sasaki, and H. Mimura, Mechanism of highly efficient electron emission from a graphene/oxide/semiconductor structure, ACS Appl. Electron. Mater. **2**, 2265 (2020).
[27] G. Hassink, R. Wanke, I. Rastegar, W. Braun, C. Stephanos, P. Herlinger, J. H. Smet, and J. Mannhart, Transparency of graphene for low-energy electrons measured in a vacuum-triode setup, APL Mater. **3**, 076106 (2015).
[28] C. Alvarado Chavarin, C. Strobel, J. Kitzmann, A. Di Bartolomeo, M. Lukosius, M. Albert, J. Bartha, and C. Wenger, Current modulation of a heterojunction structure by an ultra-thin graphene base electrode, Materials **11**, 345 (2018).
[29] Z. Li and X. Wei, A high-efficiency electron-emitting diode based on horizontal tunneling junction, IEEE Electron Device Lett. **40**, 1201 (2019).
[30] K. Murakami, T. Igari, K. Mitsuishi, M. Nagao, M. Sasaki, and Y. Yamada, Highly monochromatic electron emission from graphene/hexagonal boron nitride/Si heterostructure, ACS Appl. Mater. Interfaces **12**, 4061 (2020).
[31] R. Geick, C. H. Perry, and G. Rupprecht, Normal modes in hexagonal boron nitride, Phys. Rev. **146**, 543 (1966).
[32] K. Watanabe, T. Taniguchi, and H. Kanda, Direct-bandgap properties and evidence for ultraviolet lasing of hexagonal boron nitride single crystal, Nat. Mater. **3**, 404 (2004).
[33] C. R. Dean, A. F. Young, I. Meric, C. Lee, L. Wang, S. Sorgenfrei, K. Watanabe, T. Taniguchi, P. Kim, K. L. Shepard, and J. Hone, Boron nitride substrates for high-quality graphene electronics, Nat. Nanotechnol. **5**, 722 (2010).
[34] W. Yang, et al., Epitaxial growth of single-domain graphene on hexagonal boron nitride, Nat. Mater. **12**, 792 (2013).
[35] P. Sutter and E. Sutter, Thickness determination of few-layer hexagonal boron nitride films by scanning electron microscopy and Auger electron spectroscopy, APL Mater. **2**, 092502 (2014).

[36] H. Shinotsuka, S. Tanuma, C. J. Powell, and D. R. Penn, Calculations of electron inelastic mean free paths. XII. data for 42 inorganic compounds over the 50eV to 200keV range with the full penn algorithm, Surf. Interface Anal. **51**, 427 (2019).

[37] S. M. Sze and Kowok K. Ng, *Physics of Semiconductor Devices* (John Wiley & Sons, Inc., Hoboken New Jersey, 2007).

[38] Y.-N. Xu and W. Y. Ching, Calculation of ground-state and optical properties of boron nitrides in the hexagonal, cubic, and wurtzite structures, Phys. Rev. B. **44**, 7787 (1991).

[39] T. H. DiStefano and M. Shatzkes, Dielectric instability and breakdown in wide bandgap insulators, J. Vac. Sci. Technol. **12**, 37 (1975).

[40] G. Wu, Z. Li, Z. Tang, D. Wei, G. Zhang, Q. Chen, L.-M. Peng, and X. Wei, Silicon oxide electron-emitting nanodiodes, Adv. Electron. Mater. **4**, 1800136 (2018).

[41] J. F. Verweij and J. H. Klootwijk, Dielectric breakdown I: A review of oxide breakdown, Microelectronics J. **27**, 611 (1996).

[42] L. W. Swanson and L. C. Crouser, Total-energy distribution of field-emitted electrons and single-plane work functions for tungsten, Phys. Rev. **163**, 622 (1967).

[43] S. Jung, M. Park, J. Park, T.-Y. Jeong, H.-J. Kim, K. Watanabe, T. Taniguchi, D. H. Ha, C. Hwang, and Y.-S. Kim, Vibrational properties of h-BN and h-BN-graphene heterostructures probed by inelastic electron tunneling spectroscopy, Sci. Rep. **5**, 16642 (2015).

[44] D. K. Ferry, Electron transport at high fields in $\alpha$-$SiO_2$, Appl. Phys. Lett. **27**, 689 (1975).

[45] D. K. Ferry, Electron transport and breakdown in $SiO_2$, J. Appl. Phys. **50**, 1422 (1979).